

# Extreme ultraviolet high-harmonic spectroscopy of solids

T. T. Luu<sup>1\*</sup>, M. Garg<sup>1\*</sup>, S. Yu. Kruchinin<sup>1</sup>, A. Moulet<sup>1</sup>, M. Th. Hassan<sup>1</sup> & E. Goulielmakis<sup>1</sup>

**Extreme ultraviolet (EUV) high-harmonic radiation<sup>1,2</sup> emerging from laser-driven atoms, molecules or plasmas underlies powerful attosecond spectroscopy techniques<sup>3–5</sup> and provides insight into fundamental structural and dynamic properties of matter<sup>6,7</sup>. The advancement of these spectroscopy techniques to study strong-field electron dynamics in condensed matter calls for the generation and manipulation of EUV radiation in bulk solids, but this capability has remained beyond the reach of optical sciences. Recent experiments<sup>8,9</sup> and theoretical predictions<sup>10–12</sup> paved the way to strong-field physics in solids by demonstrating the generation and optical control of deep ultraviolet radiation<sup>8</sup> in bulk semiconductors, driven by femtosecond mid-infrared fields or the coherent up-conversion of terahertz fields to multi-octave spectra in the mid-infrared and optical frequencies<sup>9</sup>. Here we demonstrate that thin films of SiO<sub>2</sub> exposed to intense, few-cycle to sub-cycle pulses give rise to wideband coherent EUV radiation extending in energy to about 40 electronvolts. Our study indicates the association of the emitted EUV radiation with intraband currents of multi-petahertz frequency, induced in the lowest conduction band of SiO<sub>2</sub>. To demonstrate the applicability of high-harmonic spectroscopy to solids, we exploit the EUV spectra to gain access to fine details of the energy dispersion profile of the conduction band that are as yet inaccessible by photoemission spectroscopy in wide-bandgap dielectrics. In addition, we use the EUV spectra to trace the attosecond control of the intraband electron motion induced by synthesized optical transients. Our work advances lightwave electronics<sup>5,13–15</sup> in condensed matter into the realm of multi-petahertz frequencies and their attosecond control, and marks the advent of solid-state EUV photonics.**

Coherent radiation, emerging from the nonlinear interaction of intense lasers with matter, contains information about structure and dynamics and has lent itself to a wide range of fundamental spectroscopy techniques<sup>3,16</sup>. In strong-field laser physics<sup>3</sup>, acceleration of electron wavepackets<sup>17</sup> launched by the strong-field ionization<sup>18</sup> of atoms or molecules and their re-collision with their parent ions gives rise to coherent attosecond EUV radiation<sup>1,2</sup>. Such radiation can provide detailed information about electronic structure<sup>19</sup>, the atomic motion in molecules<sup>20,21</sup>, and the dynamics of free<sup>7</sup> and bound<sup>22</sup> electron wavepackets in the generated ionic species. Here we demonstrate the extension of strong-field EUV spectroscopy and photonics to the condensed phase.

In our experiments, thin ( $\sim 120$  nm), free-standing, polycrystalline SiO<sub>2</sub> films (see Supplementary Information section I) were exposed to intense field-sculpted, ultrafast optical waveforms generated in a second-generation light field synthesizer (refs 23 and 24 and M.Th.H. *et al.*, manuscript in preparation). In Fig. 1c we show spectra of the radiation emerging from the bulk of the SiO<sub>2</sub> samples (Fig. 1b) when driven by the field of a 1.5-cycle pulse (Fig. 1a; energy  $\sim 0.5$   $\mu$ J) as a function of the transmitted field amplitude that was varied in the range  $\sim 0.7$ – $1.1$  V  $\text{\AA}^{-1}$  (in the bulk of SiO<sub>2</sub>). Regularly spaced spectral peaks, the energy of which match well the odd harmonics of the ultrashort

pulse carrier frequency, attest to the coherence between the driving and emitted EUV fields.

A gradual increase in the field strength of the optical pulse gives rise to the formation of a robust spectral plateau extending over more than  $\sim 20$  eV (15–35 eV) in the EUV range. The cutoff energy, defined as the last harmonic peak discernible at the high-energy end of the EUV spectral plateau, undergoes a linear increase with optical field strength (Fig. 1d). The intensity yield of the emitted harmonic radiation exhibits a highly nonlinear dependence on optical bias, unique for each individual harmonic peak (Fig. 1e–g). The slope of the intensity yield declines at higher optical biasing of the medium (Fig. 1e), while for some of the harmonic peaks, it rises again with further increase of the field strength (Fig. 1f, g).

The linear scaling of the harmonic cutoff energy with the field amplitude distinguishes the underlying mechanism of high-harmonic radiation from that in a gas phase<sup>17</sup>, agrees with the scaling observed in previous studies of coherent, laser-driven dynamics in solids giving rise to radiation in the terahertz<sup>25</sup>, optical<sup>9</sup> and vacuum ultraviolet<sup>8</sup> ranges, and dictates the need for theoretical modelling tailored to describe the interaction of intense optical fields with bulk solids. To gain insight into the physical dynamics underlying EUV emission in our experiments, we conducted both semiclassical<sup>10</sup> and quantum-mechanical simulations<sup>11</sup> under the precise experimental conditions given above.

In the tight-binding model beyond the nearest-neighbour approximation, the dependence of energy  $E_i(k)$  in the  $i$ th band on crystal momentum  $k$  is represented by a series of spatial harmonics:

$$E_i(k) = \sum_{n=0}^{n_{\max}} \varepsilon_{i,n} \cos(nka) \quad (1)$$

Here  $a$  is the lattice constant,  $n$  is the lattice site number (order of the spatial harmonic),  $n_{\max}$  is the maximum number of distant neighbours included in the model,  $\varepsilon_{i,n}$  are Fourier coefficients, and  $\varepsilon_{i,0}$  is the band offset (see Supplementary Information section II). The highest characteristic distance in the crystal is, therefore,  $R_{\max} = n_{\max}a$ . Consequently, the maximum energy that an electron wavepacket can acquire from the field is  $E_{\max} = eF_0R_{\max} = n_{\max}\hbar\omega_B$ , where  $\omega_B = eF_0a/\hbar$  is the Bloch frequency and  $F_0$  is the field amplitude.

To illustrate the role of the energy dispersion of the lowest conduction band in the emission of EUV radiation, we first perform semiclassical simulations of a pre-existing wavepacket driven by the electric field in Fig. 1a, for  $F_0 = 0.8$  V  $\text{\AA}^{-1}$  along the contour of different spatial components, which are included in the Fourier series (equation (1)) of the band dispersion (Fig. 2b); see Supplementary Information section VIII for the case of  $F_0 = 1.1$  V  $\text{\AA}^{-1}$ . In our simulations, the amplitudes  $\varepsilon_{c,m}$ , as well as the number of significant spatial harmonics, are derived from the Fourier expansion of the band along the  $\Gamma$ –M direction in the Brillouin zone (see Supplementary Information section II). The simulations (Fig. 1d) highlight the gradual increase of the cutoff energy with spatial harmonic order  $n$  and suggest that, under our experimental conditions, deceleration of electrons by the spatial harmonics of orders

<sup>1</sup>Max-Planck-Institut für Quantenoptik, Hans-Kopfermann-Strasse 1, D-85748 Garching, Germany.

\*These authors contributed equally to this work.

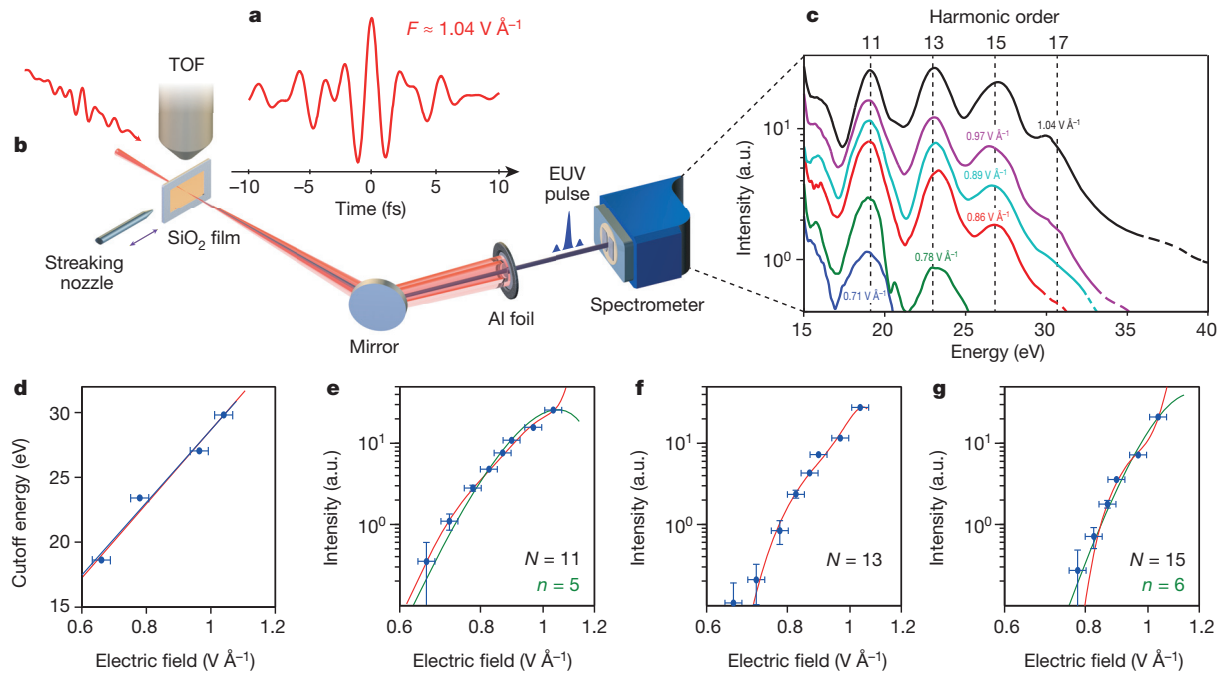


**Figure 1 | Generation, energy cutoff and intensity scaling of coherent EUV radiation in SiO<sub>2</sub> films.** **a**, The 1.5-cycle driving pulse (with spectral range  $\Delta_L \approx 1.1$ –2.5 eV) produced in a light field synthesizer and characterized by attosecond streaking, before being focused onto a thin film of SiO<sub>2</sub> (~120 nm) to generate EUV radiation (**b**). **c**, EUV spectra recorded for increasing field strengths for which the screening factor (~0.8) derived from the Fresnel formula is taken into account. The dashed portion of the curves indicates the noise floor. **d**, Scaling of the cutoff energy  $E_{\text{cutoff}}$  (blue dots with error bars) with the field amplitude  $F_0$ . Shown is linear fitting of the measured data (blue line) and results of semiclassical simulations

(red line). **e–g**, Yield dependence for harmonics of order  $N = 11$  (**e**), 13 (**f**) and 15 (**g**) on the field amplitude (blue dots). Red curves represent fittings based on equation (3), including all spatial harmonics up to  $n_{\text{max}}$ . Green curves in **e**, **g**, represent the fitting of experimental data with equation (3), where only one spatial harmonic ( $n = 5$  and  $n = 6$ , respectively) was taken into account. Error bars depict the standard deviations of the values extracted from several data sets recorded under identical conditions. Corresponding slopes of the intensity curves at  $0.7 \text{ V } \text{\AA}^{-1}$  are evaluated as  $\sim F_0^{10}$ ,  $\sim F_0^{18}$ , and  $\sim F_0^{15}$ , respectively.

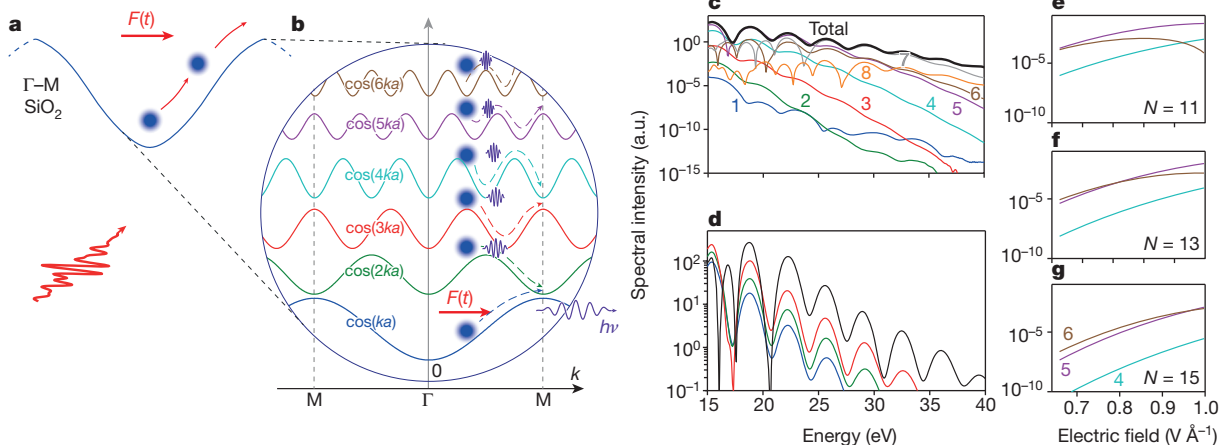


**Figure 2 | Semiclassical picture of the field-driven electron dynamics in SiO<sub>2</sub>.** **a**, An electron wavepacket driven by the field in the lowest conduction band along the  $\Gamma$ – $M$  direction of the Brillouin zone. **b**, Spatial harmonic components of the band dispersion resulting from equation (15) in Supplementary Information. Relative amplitudes are scaled, for clarity. **c**, Contributions to the EUV spectra from each of the spatial harmonics for the field of Fig. 1a at the amplitude  $F_0 = 0.8 \text{ V } \text{\AA}^{-1}$ . The total emitted spectrum

(black curve) aggregates contributions from all spatial harmonics. **d**, Simulated spectra for the electric field waveform (Fig. 1a) for the realistic band shown in **a** as a function of the peak field strength  $F_0$ . Colour-coding corresponds to field strengths of Fig. 1c. **e–g**, Contributions of spatial harmonics  $n = 4, 5, 6$  to the intensity yields of EUV harmonics of orders  $N = 11$  (**e**), 13 (**f**) and 15 (**g**) versus field amplitude  $F_0$ .

$n = 5, 6$ , and 7 play a central role in the emission of radiation near the cutoff energy.

From the linear fitting of experimental data (Fig. 1d, blue line), we evaluate the largest characteristic distance significantly contributing to the spectral intensity as  $R_{\text{cutoff}} = n_{\text{cutoff}} a = e^{-1} dE_{\text{cutoff}}/dF_0$ , and obtain

$R_{\text{cutoff}} \approx 30 \text{ \AA}$  and  $n_{\text{cutoff}} = 6.2 \pm 0.5$ .  $R_{\text{cutoff}}$  is smaller than the average size of the crystalline domain (which is  $> 40 \text{ \AA}$ ), and thus, a scattering at domain edges can be neglected (see Supplementary Information section I). Extrapolation of the linear fitting to the zero field  $F_0 = 0$  yields a cutoff energy  $E_{\text{cutoff}} = 0.6 \pm 2.0 \text{ eV}$  (see Supplementary

Information section III) and even further strengthens the link between the emitted radiation and the induction of intraband currents considered in the semiclassical treatment, where  $E_{\text{cutoff}} = 0$  for  $F_0 = 0$  is predicted. When performed under the realistic energy dispersion of the lowest conduction band  $E_c(k)$  along the  $\Gamma$ -M direction (Fig. 2a), the semiclassical simulation yields a reasonable reproduction (Fig. 2d) of the experimental spectra shown in Fig. 1c. The calculated maximum cutoff energy  $E_{\text{cutoff}} \approx 33$  eV (within the same dynamic range of our experiments), its linear scaling versus field amplitude  $F_0$ , and  $n_{\text{cutoff}} = 6$  evaluated from the slope of the cutoff dependence of the simulated spectra (red line, Fig. 1d) are in excellent agreement with our experimental findings (blue line, Fig. 1d). Simulations assuming that the field polarization is parallel to the  $\Gamma$ -K or  $\Gamma$ -A directions of SiO<sub>2</sub> yielded EUV spectra of an order of magnitude weaker intensity and lower cutoff energy in comparison to those along the  $\Gamma$ -M direction (see Supplementary Information section II, Supplementary Fig. 2). The contribution of the highest valence bands was also found to be negligible (see Supplementary Information section II). The above conclusions support the notion that, in our experiments, the EUV emission primarily occurs due to acceleration of first conduction band electrons in microcrystals, for which the  $\Gamma$ -M direction is parallel to the laser polarization axis.

In our quantum-mechanical simulations based on the numerical solution of the semiconductor Bloch equations<sup>9,11</sup>, we find that the cutoff energy and fine details of our experimental spectra are reasonably reproduced by the intraband current only, but they disagree with those obtained from interband or total polarization (see Supplementary Information section IV, Supplementary Figs 8, 9). These results were further verified by contrasting the intensity dependence of the 11th harmonic in our experiment with that predicted by the semiclassical model and interband and intraband terms of quantum-mechanical simulations (see Supplementary Information section V).

The previous comparison of simulations with measurements pinpoints the importance of intraband dynamics in describing the process and the capability of the semiclassical approach to capture key aspects of the emission of EUV radiation, including the nonlinearity pertaining to the intensity scaling. As a result, the characteristics of the EUV spectra offer direct insight into the generation of multi-PHz field-tunable intraband currents, whose cutoff frequency is adjustable from  $\nu_{\text{cutoff}} \approx 3.6$  PHz to 8.5 PHz (Fig. 1c). These are the highest frequency currents so far induced in a solid medium by optical fields, and more than an order of magnitude higher than those in previous experiments in solid-state lightwave electronics<sup>13–15</sup>.

The semiclassical theory of high-harmonic radiation<sup>26</sup> predicts that the intensity of the emitted spectra in the case of a cosine band exhibits an extreme nonlinearity versus the field amplitude  $F_0$ . For an electric field carried at a frequency  $\omega_L$ , the intensity dependence of the  $N$ th order harmonic is proportional to

$$I_N \propto (N\omega_L)^2 \left| J_N \left[ \frac{eF_0 a}{\hbar\omega_L} \right] \right|^2 \quad (2)$$

where  $J_N(z)$  is the Bessel function of the first kind of order  $N$ .

For a band whose dispersion profile comprises a few spatial harmonics, equation (2) can be generalized (see Supplementary Information section II) to account for the contributions of distant neighbours to the yield of the  $N$ th harmonic peak as

$$I_{c,N} \propto (N\omega_L)^2 \left| \sum_{n=1}^{n_{\text{max}}} n \varepsilon_{c,n} J_N \left[ \frac{n\omega_B}{\omega_L} \right] \right|^2 \quad (3)$$

These equations are also accurate in the short pulse limit with the difference that, in this case,  $F_0$  refers to the peak field strength of the pulse. Figure 2e–g illustrates how the representative spatial harmonics ( $n = 4, 5, 6$ ) influence the yield dependence of EUV harmonic peaks in our spectral range versus  $F_0$  according to equation (3). These plots underpin the possibility of extracting structural information about the

underlying medium by fitting the yield of a single or several EUV harmonic peaks by equation (3). Indeed, a simultaneous fitting for harmonic orders 11 to 15 (see Fig. 1e–g, red curves) by equation (3) yields an excellent regression and allows for retrieval of the amplitudes  $\varepsilon_{c,n}$  in expansion (1).

Based on the confidence interval of the reconstruction, our fitting reveals that the intensity dependence of EUV harmonics in the spectral range of our study aggregates primarily the contributions of EUV photons emitted when the field-driven electron wavepacket is decelerated by the spatial harmonics  $n = 5$  and 6. For instance, the yield of EUV harmonic  $N = 11$  is dominated by the deceleration of the wavepacket by the spatial harmonic  $n = 5$  (Fig. 1e, green curve), while for  $N = 15$ , deceleration by  $n = 6$  dominates (Fig. 1g, green curve); we verify this by fitting their yield based on equation (3) for the corresponding spatial harmonics. This result is in excellent agreement with the independent conclusions of the cutoff analysis of Fig. 1d, which reveals similar sensitivity to spatial harmonics of the cutoff energy of the emitted radiation.

The evaluated ratio of the significantly contributing coefficients is  $\varepsilon_{c,5}/\varepsilon_{c,6} \approx -5.1 \pm 0.6$  and accurately matches the theoretically predicted ratio<sup>27</sup> obtained in the expansion given by equation (15) in the Supplementary Information,  $\varepsilon_{c,5}/\varepsilon_{c,6} \approx -5.6$ . This result offers additional evidence that the laser-driven intraband current accurately captures the EUV emission and, most importantly, constitutes the first measurement of the fine details of the conduction band dispersion in wide bandgap materials. Indeed, the large insulating bandgap and low mobility of photo-excited carriers prevent replenishing of the created vacancies, give rise to charging effects, which in turn make photoemission spectroscopies<sup>28</sup> impractical, and limit their reach to valence or low-lying conduction bands<sup>28</sup>. As a pure polarization spectroscopy, our approach overcomes this essential frontier and highlights the promise for a new range of studies in dielectric materials. The resolution pertinent to our technique can be estimated from the highest spatial harmonic order influencing the EUV emission as  $\pi/6a \approx 0.1 \text{ \AA}^{-1}$  (for  $n_{\text{cutoff}} = 6$ ), which is close to that of modern angular resolved photoemission spectroscopy.

In a second set of experiments, we dynamically probe the physics underlying EUV generation in the condensed phase and explore routes towards the ultrafast control of multi-PHz-scale currents by conducting measurements of EUV spectra generated by various waveforms including few-cycle, 1.5-cycle, sub-cycle and half-cycle pulses. Spectra recorded for two settings of the carrier envelope phase (CEP) of the above driving fields are shown in Fig. 3. The increase of the averaged inter-peak energy spacing (Fig. 3a to Fig. 3b) and the broadening of these harmonic peaks (Fig. 3c) are compatible with increasing driver frequencies and decreasing pulse duration of the optical field, respectively, and further corroborate the coherent relation between the emitted and driving fields. In contrast to few-cycle and 1.5-cycle driving fields (Fig. 3a, b), sub-cycle and, even more evidently, half-cycle field waveforms give rise to EUV continua (Fig. 3c, d), whose amplitude and shape show a considerable sensitivity to the CEP adjustments.

The dynamic control of the emission attained by CEP manipulation of the waveform of the driver pulses lends itself to use as an additional platform to verify the validity of the conclusions reached in the cutoff and intensity analysis (Fig. 1d–g), by further contrasting our findings with quantum-mechanical and semiclassical models. Figure 3e, f, k, l shows simulated temporal dynamics of an electron wavepacket in the conduction band of SiO<sub>2</sub> for two representative waveforms of the few-cycle and half-cycle driving fields, and for the phase settings of the insets of Fig. 3a, d. Interband dynamics give rise to periodic modulations of the amplitude of the wavepacket as a function of time, whereas the intraband dynamics are best manifested by the lateral oscillatory displacement of the excited wavepacket. Figure 3g, m depicts the simulated temporal intensity profiles of the radiation induced by intraband currents, spectrally filtered in the energy range of our experiments ( $>15$  eV); Fig. 3h, n shows the results of semiclassical simulations;

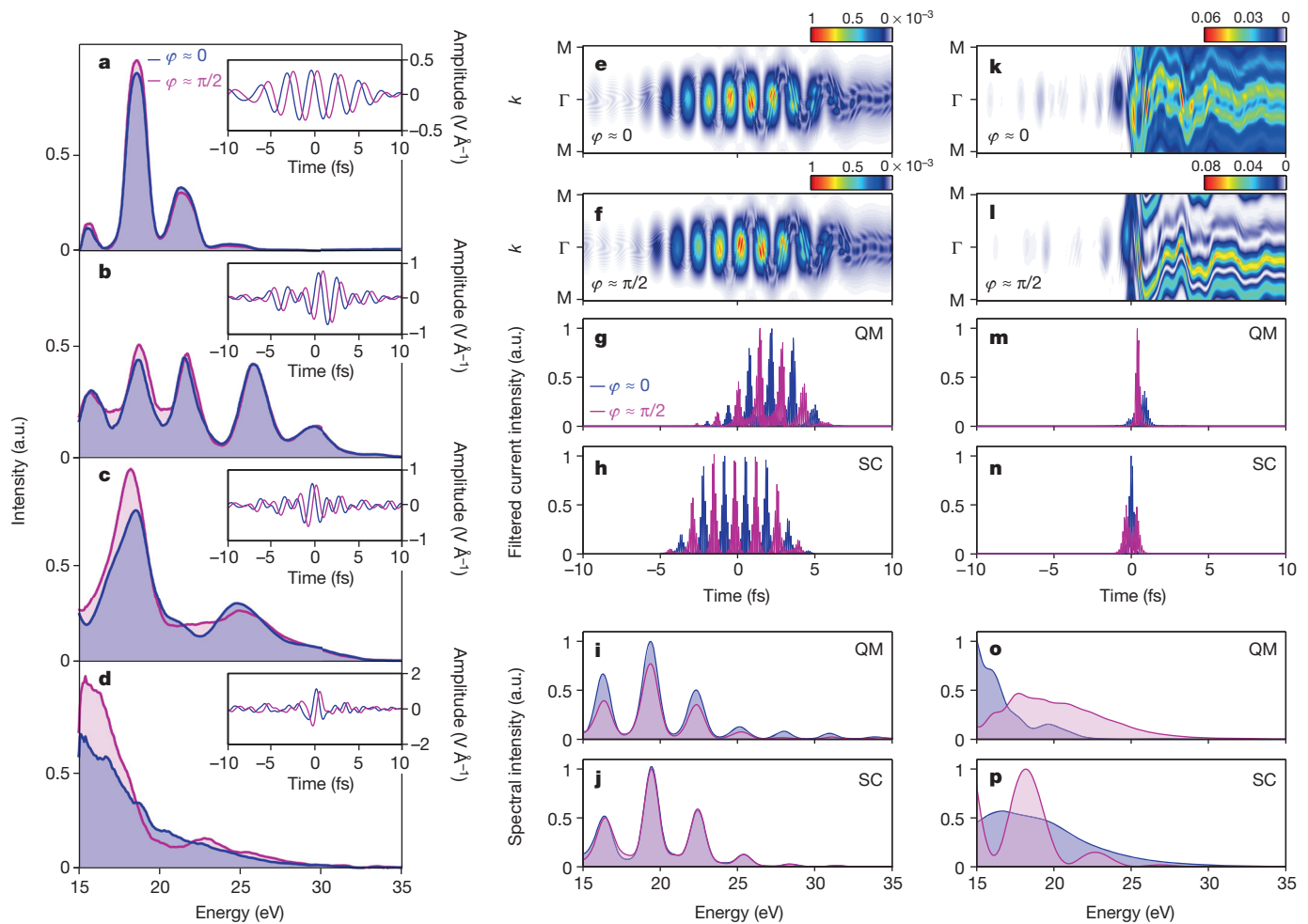


**Figure 3 | Field control of laser-driven EUV emission in SiO<sub>2</sub> (experiment and simulation).** **a–d**, EUV harmonic spectra recorded for two CEP settings ( $\varphi_{\text{CE}} \approx 0$ , blue;  $\varphi_{\text{CE}} \approx \pi/2$  rad, magenta) of the driving waveforms shown in insets: **a**, few-cycle ( $A_L \approx 1.1$ – $1.8$  eV and carrier frequency  $\omega_L \approx 1.52$  eV), **b**, 1.5-cycle ( $A_L \approx 1.1$ – $2.5$  eV,  $\omega_L \approx 1.96$  eV), **c**, sub-cycle ( $A_L \approx 1.1$ – $3.1$  eV,  $\omega_L \approx 2.227$  eV), and **d**, half-cycle ( $A_L \approx 1.1$ – $4.6$  eV,  $\omega_L \approx 2.1$  eV) pulses. The waveforms are sampled by attosecond streaking. **e, f**, Population dynamics in the lowest conduction band of SiO<sub>2</sub> along the  $\Gamma$ –M direction driven by the few-

cycle pulse with  $\varphi_{\text{CE}} \approx 0$  and  $\varphi_{\text{CE}} \approx \pi/2$  rad, respectively (insets of **a**). **g, h**, Temporal intensity profiles  $I(t) \propto |\partial J(t)/\partial t|^2$  of the radiated EUV fields in the spectral region  $> 15$  eV for a few-cycle pulse, calculated with quantum-mechanical (QM) and semiclassical (SC) models.  $J(t)$  denotes the intraband current. **i, j**, Corresponding spectra obtained from quantum-mechanical and semiclassical simulations for a few-cycle pulse for the above-mentioned CEP settings are marked by the same colour code. **k–p**, Same as **e–j** but calculated for a half-cycle pulse (insets of **d**).

and Fig. 3i, j, o, p show the corresponding spectra (see Supplementary Information section IV for additional information). Importantly and in support of the conclusions of the intensity scaling analysis, the results of the semiclassical simulations for the entire range of pulse waveforms exploited are virtually identical, if we consider the band dispersion with the terms  $\sim \cos(5ka) - 0.19\cos(6ka)$ , which represent significantly contributing spatial harmonics and their experimentally retrieved relative amplitudes (Fig. 1d–g).

The reasonable reproduction of the experimental spectra for the broad range of waveforms used (see also Supplementary Information section IV) by both the semiclassically and quantum-mechanically simulated intraband currents allows the linking of the temporal electron dynamics underlying our simulations with those in our experiments. For few-cycle pulses (Fig. 3g), excitation of the currents and concomitant radiation extend temporally over several field cycles. The current profile (Fig. 3g, h, red and blue curves) in this case is temporally displaced by a CEP variation of the optical driving field, but its structure remains virtually unaffected, resulting in nearly invariable spectra (Fig. 3i, j) with respect to the variation of this pulse parameter, in agreement with our experiments (Fig. 3a). By contrast, half-cycle pulses confine and control electric currents to the optical cycle

(Fig. 3m, n) with CEP. This control is manifested in the spectral domain by wideband modulations of the broadband emitted spectra (Fig. 3o, p) and their continuum shape to give structured ones in accordance with our experiments (Fig. 3d). Notably, the semiclassical simulation (Fig. 3j, p) seems to reproduce this trend better than the quantum-mechanical one (Fig. 3i, o). This can be attributed to the fact that intraband current and interband polarization are inherently coupled in the semiconductor Bloch equations.

The CEP-based manipulation of the emitted spectra emanating from an extreme nonlinear process has served for years as a paradigm of sub-cycle confinement and control in attosecond physics<sup>6,13</sup>. Our experiments and simulations support the notion that this paradigm is also applicable for strong-field-driven electron dynamics and EUV emission in bulk solids. As half-cycle drivers are confined to a *de facto* sub-femtosecond interval (duration  $\tau_p < 1$  fs), these broadband spectral modulations offer evidence of the attosecond control of the induced multi-PHz intraband currents, and represent a unique and generic tool for tracing coherent strong-field dynamics in solids.

Further study of the coherence of the emitted EUV radiation included the measurement of the far-field spatial properties of the emerging radiation. The measurements reveal a well-behaved (ellipti-

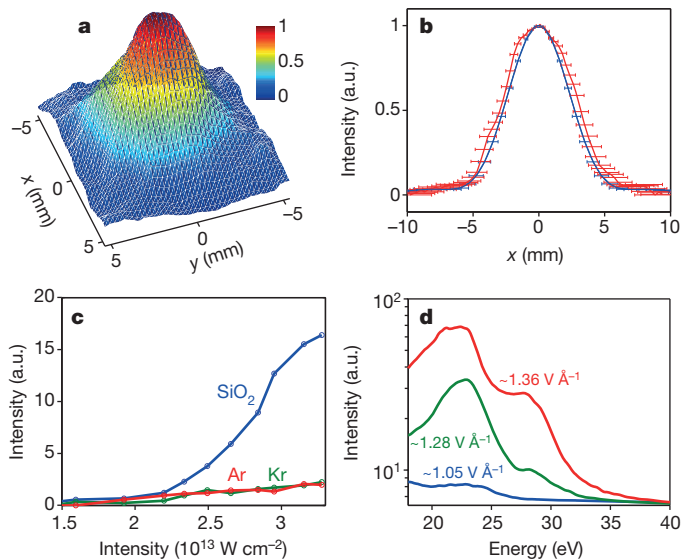


**Figure 4 | Coherent EUV source characteristics.** **a**, Far-field spatial intensity profile of the EUV beam sampled by a detector placed at a distance of  $\sim 90$  cm downstream from the source. **b**,  $x$ -axis profile (red curve) of **a**, and far-field EUV beam profile (blue curve) calculated with semiclassical simulations and free-space propagation. Error bars depict the standard deviations of the values extracted from several data sets recorded under identical conditions. **c**, EUV photon yield (1.5-cycle pulse) integrated over the range (15–40 eV) for SiO<sub>2</sub> (blue curve) and for the noble gases Ar (red curve) and Kr (green curve). **d**, EUV supercontinua in SiO<sub>2</sub> extending to  $\sim 40$  eV driven by half-cycle pulses at different peak field strengths (given on curves).

city  $\sim 0.93$ ) EUV beam profile (Fig. 4a), whose dimensions and shape are in excellent agreement with those predicted by our semiclassical simulations and free-space propagation (Fig. 4b, blue curve), and suggest the full spatial coherence of the emitted EUV (see Supplementary Information section VI).

To gain insights into the conversion efficiency of laser radiation to extreme ultraviolet, we compared the yield of the EUV emission in SiO<sub>2</sub> with that of two broadly used media in gas-phase attosecond physics, Kr and Ar (Fig. 4c), under identical conditions (see Supplementary Information section VII). Our study reveals that the yield of EUV emission from SiO<sub>2</sub>, which is approximately 8 times higher than that of these gases in the range of applied optical fields (Fig. 1c), falls within a similar efficiency class ( $10^{-7}$ – $10^{-6}$ ) as that of gases<sup>29</sup>.

Extension of the EUV continua to higher photon energies (up to 40 eV or  $\nu \approx 9.7$  PHz) is also possible by applying stronger field ( $\sim 1.36 \text{ V \AA}^{-1}$ ) to our samples (Fig. 4d). For an even stronger optical field, the ultrathin samples show degradation due to physical melting. However, tests on thicker samples showed suppression of melting effects and may soon enable advancement of the coherent emission towards the soft X-ray regime, catalysing further developments.

The generation of broadband EUV radiation by driving the coherent nonlinear motion of electrons in bulk solids advances attosecond high-harmonic spectroscopy to the condensed phase, and promotes solid-state laser photonics and electronics to a new frequency regime with great potential for novel scientific and technological inquiry. It offers new possibilities for the tracing and attosecond control of strong-field electron dynamics in solids.

Received 22 June 2014; accepted 27 March 2015.

- Ferry, M. *et al.* Multiple-harmonic conversion of 1064 nm radiation in rare gases. *J. Phys. B* **21**, L31–L35 (1988).
- L'Huillier, A. & Balcou, P. High-order harmonic generation in rare gases with a 1-ps 1053-nm laser. *Phys. Rev. Lett.* **70**, 774–777 (1993).
- Corkum, P. B. & Krausz, F. Attosecond science. *Nature Phys.* **3**, 381–387 (2007).
- Hentschel, M. *et al.* Attosecond metrology. *Nature* **414**, 509–513 (2001).
- Goulielmakis, E. *et al.* Attosecond control and measurement: lightwave electronics. *Science* **317**, 769–775 (2007).
- Baltuška, A. *et al.* Attosecond control of electronic processes by intense light fields. *Nature* **421**, 611–615 (2003).
- Remetter, T. *et al.* Attosecond electron wave packet interferometry. *Nature Phys.* **2**, 323–326 (2006).
- Ghimire, S. *et al.* Observation of high-order harmonic generation in a bulk crystal. *Nature Phys.* **7**, 138–141 (2011).
- Schubert, O. *et al.* Sub-cycle control of terahertz high-harmonic generation by dynamical Bloch oscillations. *Nature Photon.* **8**, 119–123 (2014).
- Feise, M. W. & Citrin, D. S. Semiclassical theory of terahertz multiple-harmonic generation in semiconductor superlattices. *Appl. Phys. Lett.* **75**, 3536–3538 (1999).
- Golde, D., Meier, T. & Koch, S. W. High harmonics generated in semiconductor nanostructures by the coupled dynamics of optical inter- and intraband excitations. *Phys. Rev. B* **77**, 075330 (2008).
- Mücke, O. D. Isolated high-order harmonics pulse from two-color-driven Bloch oscillations in bulk semiconductors. *Phys. Rev. B* **84**, 081202 (2011).
- Krüger, M., Schenk, M. & Hommelhoff, P. Attosecond control of electrons emitted from a nanoscale metal tip. *Nature* **475**, 78–81 (2011).
- Schiffrin, A. *et al.* Optical-field-induced current in dielectrics. *Nature* **493**, 70–74 (2013).
- Schultze, M. *et al.* Controlling dielectrics with the electric field of light. *Nature* **493**, 75–78 (2013).
- Levenson, M. D. & Kano, S. *Introduction to Nonlinear Laser Spectroscopy* Revised edn (Academic, 1988).
- Corkum, P. B. Plasma perspective on strong-field multiphoton ionization. *Phys. Rev. Lett.* **71**, 1994–1997 (1993).
- Keldysh, L. V. Ionization in field of a strong electromagnetic wave. *Sov. Phys. JETP* **20**, 1307–1314 (1965).
- Itatani, J. *et al.* Tomographic imaging of molecular orbitals. *Nature* **432**, 867–871 (2004).
- Baker, S. *et al.* Probing proton dynamics in molecules on an attosecond time scale. *Science* **312**, 424–427 (2006).
- Wörner, H. J., Bertrand, J. B., Kartashov, D. V., Corkum, P. B. & Villeneuve, D. M. Following a chemical reaction using high-harmonic interferometry. *Nature* **466**, 604–607 (2010).
- Smirnova, O. *et al.* High harmonic interferometry of multi-electron dynamics in molecules. *Nature* **460**, 972–977 (2009).
- Hassan, M. T. *et al.* Attosecond photonics: synthesis and control of light transients. *Rev. Sci. Instrum.* **83**, 111301 (2012).
- Wirth, A. *et al.* Synthesized light transients. *Science* **334**, 195–200 (2011).
- Waschke, C. *et al.* Coherent submillimeter-wave emission from Bloch oscillations in a semiconductor superlattice. *Phys. Rev. Lett.* **70**, 3319–3322 (1993).
- Wegener, M. *Extreme Nonlinear Optics: An Introduction* (Springer, 2005).
- Chelikowsky, J. R. & Schlüter, M. Electron states in  $\alpha$ -quartz: a self-consistent pseudopotential calculation. *Phys. Rev. B* **15**, 4020–4029 (1977).
- Damaselli, A. Probing the electronic structure of complex systems by ARPES. *Phys. Scr. T* **109**, 61–74 (2004).
- Cabasse, A., Machinet, G., Dubrouil, A., Cormier, E. & Constant, E. Optimization and phase matching of fiber-laser-driven high-order harmonic generation at high repetition rate. *Opt. Lett.* **37**, 4618–4620 (2012).

Supplementary Information is available in the online version of the paper.

**Acknowledgements** We thank M. Wismer for support in calculations, and A. Jain for help during experiments. This work was supported by a European Research Council grant (Attoelectronics-258501), the Deutsche Forschungsgemeinschaft Cluster of Excellence: Munich Centre for Advanced Photonics (www.munich-photonics.de), the Max Planck Society and the European Research Training Network ATTOFEL.

**Author Contributions** T.T.L. and M.G. conducted the experiments; A.M. and M.Th.H. contributed to the development of the source; E.G. conceived the experiments; T.T.L., M.G. and S.Yu.K. conducted the simulations; S.Yu.K. performed the analytical derivations; E.G., T.T.L., M.G. and S.Yu.K. contributed to the preparation of the manuscript.

**Author Information** Reprints and permissions information is available at www.nature.com/reprints. The authors declare no competing financial interests. Readers are welcome to comment on the online version of the paper. Correspondence and requests for materials should be addressed to E.G. (elgo@mpq.mpg.de).